Roth, D. L., Brodsky, E. E., Finnegan, N. J., Rickenmann, D., Turowski, J., Badoux, A. (2016): Bed load sediment transport inferred from seismic signals near a river. - *Journal of Geophysical Research*, *121*, 4, pp. 725—747.

DOI: http://doi.org/10.1002/2015JF003782

AGU PUBLICATIONS

JGR

Journal of Geophysical Research: Earth Surface

RESEARCH ARTICLE
10.1002/2015JF003782

Key Points:
- Water turbulence, rainfall, and sediment transport generate seismic signals near rivers
- Component signals are isolated through linear inversion of calibration seismic spectra
- Sediment transport rates predicted using discharge, precipitation, and seismic data

Supporting Information:
- Supporting Information S1
- Figure S1
- Figure S2
- Figure S3
- Figure S4
- Figure S5
- Figure S6
- Figure S7
- Figure S8

Correspondence to:
D. L. Roth,
dlroth@ucsc.edu

Citation:
Roth, D. L., E. E. Brodsky, N. J. Finnegan, D. Rickenmann, J. M. Turowski, and A. Badoux (2016), Bed load sediment transport inferred from seismic signals near a river, *J. Geophys. Res. Earth Surf.*, *121*, 725–747, doi:10.1002/2015JF003782.

Received 6 NOV 2015
Accepted 25 MAR 2016
Accepted article online 1 APR 2016
Published online 25 APR 2016

Bed load sediment transport inferred from seismic signals near a river

Danica L. Roth[1], Emily E. Brodsky[1], Noah J. Finnegan[1], Dieter Rickenmann[2], Jens M. Turowski[3], and Alexandre Badoux[2]

[1]Department of Earth and Planetary Sciences, University of California, Santa Cruz, California, USA, [2]Snow and Landscape Research, WSL Swiss Federal Institute for Forest, Snow and Landscape Research, Birmensdorf, Switzerland, [3]GFZ German Research Centre for Geosciences, Potsdam, Germany

Abstract We examine broadband (5–480 Hz) seismic data from the Erlenbach stream in the Swiss Prealps, where discharge, precipitation, and bed load transport are independently constrained. A linear inversion of seismic spectra, exploiting isolated discharge or rain events, identifies the signals generated by water turbulence and rainfall. This allows us to remove the contributions of turbulence and rainfall from the seismic spectra, isolating the signal of bed load transport. We calibrate the regression for bed load transport during one storm and then use this regression with precipitation and discharge data to calculate bed load transport rates from 2 months of seismic spectra. Our predicted bed load transport rates correlate reasonably well with transport rates from calibrated geophones embedded in the channel ($r^2 \sim 0.6$, $p < 10^{-10}$). We find that the seismic response to rainfall is broadband (~16–480 Hz), while water turbulence and sediment transport exhibit seismic power primarily in lower frequencies (<100 Hz), likely due to longer attenuation path lengths. We use the varying attenuation at each seismometer to infer that a downstream waterfall is the primary source of the water turbulence signal. Our results indicate that deconstruction of seismic spectra from rivers can provide insight into the component signals generated by water turbulence, rainfall, and sediment transport. Further, the regression of seismic spectra with precipitation, discharge, and bed load transport data for a single calibration period enables the estimation of transport for subsequent periods with only precipitation, discharge, and seismic data. Hence, in combination with precipitation and discharge data, seismic data can be used to monitor bed load sediment transport.

1. Introduction

The transport of coarse sediment in rivers is a fundamental control on fluvial incision and channel morphology and therefore has broad implications for a wide array of fields including landscape evolution, ecology, land use management, and civil engineering. However, sediment transport is challenging to accurately monitor and predict. Currently used monitoring approaches include direct collection [e.g., *Leopold and Emmett*, 1977], recording the signals of bed load impacts with the bed using in-stream hydrophones or geophones [e.g., *Bogen and Møen*, 2003; *Gray et al.*, 2010; *Rickenmann and McArdell*, 2007; *Turowski et al.*, 2009, 2011], the use of tracer or radio frequency identification particles [e.g., *Schneider et al.*, 2014; *Wilcock*, 1997], and calculation via empirical relationships calibrated in the laboratory [e.g., *Wilcock and Crowe*, 2003; *Meyer-Peter and Müller*, 1948]. In situ measurement techniques can be logistically challenging and cost prohibitive, especially during large floods when the majority of coarse sediment transport occurs. In-stream monitoring also risks damage to or loss of expensive instrumentation, as well as potential contamination of data due to altered stream flow and transport patterns around equipment.

The nonlinearity and stochasticity of sediment transport and its dependence on a multitude of dynamic local variables also limit the accuracy of transport estimates extrapolated from existing data. Empirical relationships calculated from data obtained in laboratory experiments, or even at low flows in rivers, can fail to accurately represent real, large-scale transport events during higher flows, while data measured over short timescales can be at odds with long-term transport rates [e.g., *Bunte and Abt*, 2005; *Recking et al.*, 2012]. These shortcomings highlight the need for monitoring methods that are able to collect high-resolution sediment transport data over a wide range of conditions and timescales.

Growing support for continuous, low-cost and noninvasive measurement techniques has led to promising research into monitoring bed load transport via the elastic waves generated by sediment as it impacts the

river bed during transport. *Burtin et al*. [2008] found that 1–20 Hz seismic signals near the Trisuli River in Nepal corresponded closely with river discharge. Several studies have found hysteresis in seismic power versus discharge or stage over timescales ranging from individual flood events to seasons, which was attributed to sediment transport [e.g., *Govi et al*., 1993; *Hsu et al*., 2011; *Burtin et al*., 2008, *Burtin et al*., 2010; *Schmandt et al*., 2013; *Chao et al*., 2015; *Barrière et al*., 2015]. On the Chijiawan River in Taiwan, *Roth et al*. [2014] showed that seismic hysteresis correlated strongly with sediment transport rates and used a metric for seismic hysteresis to track the downstream migration of a sediment pulse released following a dam removal. Several studies have also delved more quantitatively into the spectral signature of bed load transport and found that water discharge generates seismic power in lower frequencies than bed load sediment transport [e.g., *Burtin et al*., 2011; *Schmandt et al*., 2013; *Barrière et al*., 2015]. *Tsai et al*. [2012] developed a theoretical model for the power spectral density (PSD) of Rayleigh waves generated by saltating bed load particles, assumed to be impacting the bed vertically. *Gimbert et al*. [2014] proposed a complementary theoretical model for the seismic signal generated by turbulent water flow in a river, which also contributes strongly to the seismic PSD and hence influences the magnitude of hysteresis. This finding, in particular, provides an important motivation for obtaining high-quality measurements of bed load sediment transport rates and flow attributes in parallel with seismic data.

Here we offer a simple, empirically calibrated linear approximation model for the seismic signal generated by three components: rainfall impacting the ground, water turbulence coupling with the river bed, and coarse sediment impacting the river bed during transport. In section 2, we introduce our field site on the Erlenbach stream in Switzerland and discuss data collection and preliminary processing. In section 3, we develop our linear least squares regression model and calibrate it using bed load transport data from a single storm. We then invert our calibrated model to predict bed load transport rates during the remaining storms, using only our calibrated regression coefficients, precipitation, discharge, and seismic data. Section 4 reports the results of the above sediment transport predictions and the model calibration, which represents the normalized power spectra registered at each seismometer per unit precipitation, discharge, or bed load sediment transport rate. In section 5, we discuss the accuracy of our calibration and predictions, as well as the validity of using a linear approximation. We also use information about the signal components and attenuation to gain insight into the signal sources and impact parameters. Our results demonstrate that information about precipitation, discharge, and transport is contained in seismic spectra near rivers, and that seismic data, combined with precipitation and discharge, can therefore be used to monitor bed load sediment transport.

2. Field Site, Data Collection, and Processing Methods

2.1. The Erlenbach

The Erlenbach is a small, steep alluvial mountain stream in the Swiss Prealps (Figures 1a and 1b). See Table 1 for study reach and catchment characteristics (summarized from *Rickenmann and McArdell* [2007] and *Turowski et al*. [2009, 2011]). The channel is a step-pool morphology with occasional cascades and riffle reaches, and an average bankfull channel width of 3.7 m [*Molnar et al*., 2010], although the study reach itself is ~5 m wide. The study reach, located halfway between an upstream tributary junction and the beginning of an engineered cement-bed reach downstream, consists of alluvial and colluvial material weathered from the Wägital Flysch bedrock [*Winkler et al*., 1985], though bedrock exposures within the channel itself are rare. Most of the Erlenbach catchment is located on a large landslide complex, and sediment is supplied to the channel by highly active hillslopes [*Turowski et al*., 2011]. Grain size ranges from clay to meter-sized boulders, with $D_{50} \sim 8$ cm and $D_{90} \sim 30$ cm [*Turowski et al*., 2011]. Sediment transport is primarily driven by convective summer storms, which tend to produce flashy hydrographs [*Turowski et al*., 2011].

2.2. Sediment Transport Data

The Erlenbach possesses an extensive monitoring infrastructure (Figure 1c) with over 30 years of observations [*Rickenmann*, 1997; *Rickenmann and McArdell*, 2007; *Rickenmann and Fritschi*, 2010]. An important component of this infrastructure is the Swiss plate geophone, an indirect bed load monitoring system that has provided continuous, reliable measurements of transport in the Erlenbach since 2002 [*Turowski et al*., 2009, 2011; *Rickenmann et al*., 2012, 2014]. The bed load impact sensors consist of geophones attached to the undersides of steel plates (0.36 m × 0.5 m × 0.015 m) installed flush in the channel bed at the downstream end of a ~40 m engineered concrete reach [*Beer et al*., 2015; *Rickenmann et al*., 2012]. The steel plates are acoustically

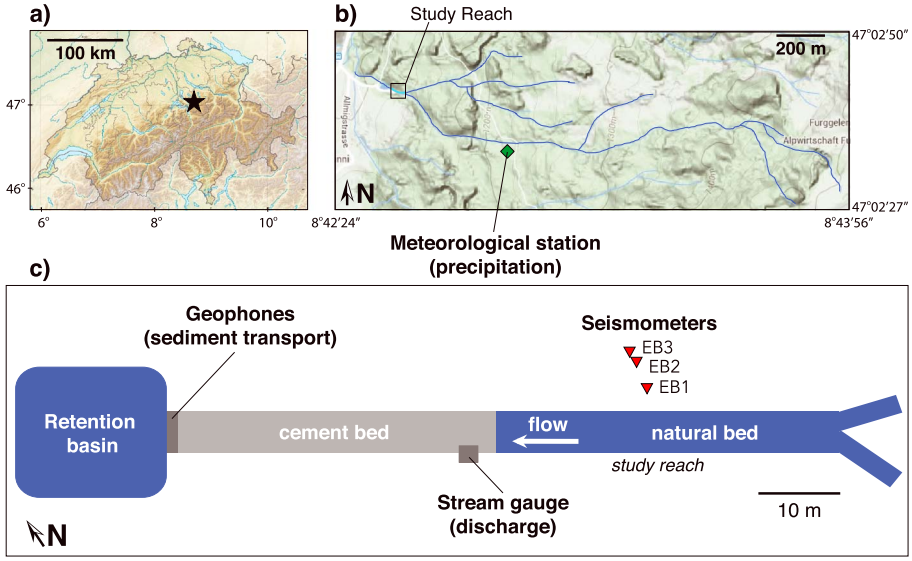

Figure 1. Field site location (a) on a map of Switzerland and (b) on the Erlenbach channel network map (study reach highlighted in box). (c) Schematic of the study reach—note that the seismometers are not aligned perpendicular to the river.

isolated from the bed and each other with elastomer elements, allowing each geophone to measure vibrations generated by direct bed load impacts upon its plate. The number of impulses (peaks exceeding a threshold value) per minute is recorded for each geophone. This threshold is set to count impacts of grains larger than ~9.5 mm [*Rickenmann et al.*, 2012]. Note that a single particle impact can cause multiple impulses. Transport in the Erlenbach is negligible below a threshold discharge of ~150 L/s and generally becomes large enough to be detected by the geophones around 300 L/s [*Turowski et al.*, 2011]. Therefore, any geophone counts during times with water discharge below 150 L/s were assumed to be noise (e.g., due to scientists working in the channel); we assume such noise may also affect the seismic data and exclude times with these spurious counts from analysis.

While previous work on the Erlenbach has utilized analog geophone data, these observations are recorded only during active transport events, when impulse and rainfall thresholds are exceeded. Here we instead use digitally recorded geophone data [*Beer et al.*, 2015], which are recorded continuously at 1 min intervals throughout the entire study period. The 1 min impulse counts were then summed over 10 min periods for this study.

Sediment budgeting and long-term volumetric flux rates are constrained at the Erlenbach with regular surveying of a sediment retention basin (Figure 1c) constructed in 1982 and located immediately downstream of the large check dam with the geophones. Bed load is also sampled during active transport events with an

Table 1. Erlenbach Study Reach Channel and Seismic Characteristics

Monitoring Period	6 July to 1 September 2013
Mean study reach elevation (meters above sea level)	1114
Study reach drainage area (km^2)	0.7
Mean study reach channel bed slope	0.1
Channel bed width (m)	5
D_{50} (cm)	8
D_{90} (cm)	30
Mean annual precipitation (mm)	2290
Mean annual runoff (mm)	1770
Mean annual sediment yield collected in retention basin (m^3)	455
Average erosion rate (mm/yr)	0.64
Discharge threshold for transport (L/s)	~150
Discharge threshold for geophone detection of transport (L/s)	~300
Substrate bulk density (kg/m^3)	~1750

Rickenmann and McArdell [2007], *Turowski et al.* [2009, 2011], *Badoux et al.* [2012], and this study

Table 2. Data Collected

	Seismic	Precipitation	Discharge	Sediment Transport
Instrument	L28 seismometers	Lambrecht tipping bucket gauge (heated)	BTL5 micropulse linear transducer (rod style)	20DX geophones
Processed data (units)	Power spectral density $((nm/s)^2/Hz)$	Rainfall (mm)	Volumetric flux (L/s)	Geophone impulses (counts)
Sampling rate	1 kHz	10 min	10 min	10 kHz impulses binned per 1 min
Distance from study reach (thalweg nearest seismometers)	EB1, 4 m; EB2, 6 m; and EB3, 7 m	~500 m upstream	~20 m downstream	~60 m downstream

automatic system (installed in 2008–2009) that moves wire mesh baskets (1 m^3 in volume) into the flow immediately downstream of the geophones, capturing sediment greater than 1 cm in diameter as it falls into the retention basin below. These systems have enabled previous studies to empirically calibrate the relationships between geophone impulses and mass or volumetric sediment flux [*Rickenmann et al*., 2012]. Laboratory experiments have also demonstrated correlation between the number of impulses and the energy transmitted to the bed by impacting particles [*Rickenmann et al*., 2014; *Turowski and Rickenmann*, 2009]. We do not think that noise from the basket samplers influences the seismic model developed here because it was active during only part of three observed transport events recorded during this study.

2.3. Discharge Data

Instantaneous stage data were collected every 10 min from a gauging station roughly 20 m downstream of the study reach (Figure 1c and Table 2) and converted into volumetric discharge using previously established calibration relations [e.g., *Beer et al*., 2015]. For this study, the average discharge during each 10 min period was then calculated as the mean of each 10 min data point and its predecessor.

2.4. Precipitation Data

Precipitation data were collected every 10 min at a meteorological station ~500 m upstream of the study reach (Figure 1b and Table 2). Data from this station have been used by previous studies to represent rainfall rates over the entire catchment [e.g., *Turowski et al*., 2009; *Badoux et al*., 2012].

2.5. Seismic Data

For the study period of 6 July to 1 September 2013, we installed three L28 broadband seismometers on the bank of the Erlenbach, ~20 m equidistant from an upstream tributary junction and the start of the engineered cement-bed reach containing the geophones (~60 m downstream) (Figure 1c and Table 2). The seismometers were positioned at the approximate midpoint of a reach ~8 m long; this was the straightest section of the channel with the fewest large boulders. The channel here has a roughly rectangular cross section, and the banks have been partially engineered and reinforced with meter-sized boulders sourced from the channel. All three instruments sampled at 1 kHz and were buried directly in the ground at centimeter depth in a line slightly off from perpendicular to the channel (due to physical obstacles, e.g., trees and boulders), at horizontal distances of 4 m, 6 m, and 7 m from the channel thalweg (Figure 1c).

Data from all three seismometers were processed into 10 min average power spectral density (PSD) over 1 Hz bands as follows. Raw time series data for seismic ground velocity were cut into 6 h segments to be detrended and demeaned, tapered at 1%, and corrected for instrument response with frequency limits 1, 4.5, 480, and 495 Hz. The 1 min average power at each frequency was then calculated using Welch's power spectral density estimate [*Welch*, 1967] with 50% overlap of 1 s windows (1000 samples), resulting in discrete 1 Hz frequency bands. These 1 min values were then summed into 10 min bins to match the precipitation, discharge, and geophone impulse count data.

3. Model

General linear least squares regressions were used to quantify the relationship between the PSD (over 1 Hz frequency bands) and each of the independently constrained processes (rainfall, water turbulence coupling with the bed, and bed load sediment transport) known to be generating seismic signals when transport occurred. Because the Erlenbach is under heavy use for both research and recreation, all analyses performed

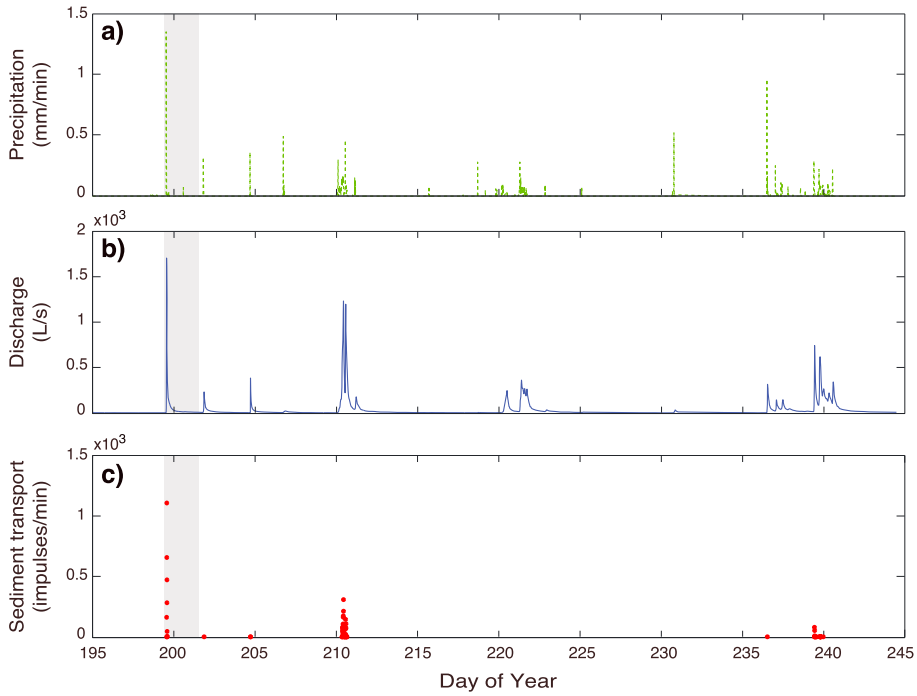

Figure 2. (a) Precipitation, (b) discharge, and (c) bed load sediment transport data for the entire season. Sediment transport training data are from the storm on day 199 (delineated with gray bars); all other transport data were used only for testing the model.

in this study maximized the signal-to-noise ratio by only using data collected during times with active processes (rainfall, elevated discharge, and/or bed load transport). Seismic data during these selected periods were controlled for quality through hand examination to filter out times with documented channel work and unaccounted noise spikes possibly caused by nearby human or wildlife activity. Within this subset of selected data, regressions were performed using precipitation and discharge data from all events over the entire 2 month installation period. However, the geophone data used for the regressions were from only a single calibration storm (18 July 2013), hereafter referred to as the model "training" data (Figure 2). These regressions were then used to calibrate a predictive least squares model for sediment transport. The model was tested using data from the remainder of the installation (excluding the training data), which we will call the "test" data (Figure 2). The intent of this approach was to maximize model accuracy while still simulating a realistic application of this method in reasonable field conditions, where precipitation and discharge tend to be more easily monitored than sediment transport.

3.1. General Linear Least Squares Regression Model

The total energy of a seismic waveform generated by multiple sources is the sum of the energy in each of the contributing signals. Hence, the total seismic PSD, $P = P_Q + P_p + P_{qs} + P_N$, is the sum of the PSDs generated by water turbulence (P_Q), rainfall (P_p), bed load sediment impacts (P_{qs}), and other noise (P_N). In constructing a linear least squares model, we further assume that, to first order, the PSD generated by each contributing process scales linearly with a variable representing the magnitude of that process (see section 5.2 for a detailed discussion of the justifications and implications of this assumption). We therefore model the total seismic PSD, $P_f(t)$, at a given time t and frequency f, as a linear combination of the seismic power generated by water discharge (Q), precipitation (p), and sediment transport (q_s), plus some frequency-dependent background noise (N_f). This background noise is likely dominated by electrical and mechanical sources not distinguishable by the hand examination above and is hence assumed to be roughly constant over time. At a single frequency, seismic power over time is thus

$$P_f(t) = a_f Q(t) + b_f p(t) + c_f q_s(t) + N_f, \quad (1)$$

where a_f, b_f, and c_f are the constant linear coefficients for each variable at frequency f. The full spectrum of coefficients a, b, and c over all frequencies represents the relative spectral contributions of water

Table 3. Conditions Used for Regressions

	Conditions for Times Used in Regression/Calculation				
Calculated Value	Discharge (Q) (L/s)	Precipitation (p) (mm/min)	Transport (q_s) (impulses/min)	Frequencies (Hz)	Other Constraints
Discharge coefficient (a_f)	any	0	0	0–500	all events
Precipitation coefficient (b_f)	<50	>0	0	0–500	all events
Transport coefficient (c_f)	>150	any	>0	0–500	calibration event only
Noise (N_f)	<3	0	0	0–500	three nights (9 P.M. to 3 A.M.)
Sediment transport ($q_{s,\mathrm{pred}}$)	>150	any	--	16–100	all events

turbulence, rainfall, and bed load impacting the bed during transport, respectively, as observed at a given seismometer. This includes coupling between the measured processes and ground velocity, as well as the effects of distance-, medium-, and frequency-dependent attenuation (i.e., the Green's function).

3.2. Multicollinearity Addressed by Regression of Independent Subsets

Multicollinearity among rain, discharge, and sediment transport represents a significant challenge in regressing a unique and independent coefficient spectrum for each process. Because all three variables covary (especially discharge and bed load transport), multiple regression can result in coefficient estimates with increased standard error, partial dependence on the wrong variables, and oversensitivity to minor outliers or noise within the data.

Fortunately, however, rain storms and subsequent periods with elevated discharge in the Erlenbach catchment tend to be brief and flashy: rainfall often ceases by the time peak discharge is reached at the study reach, resulting in time separation between rain and elevated discharge events. Instead of using a single multiple regression, we were therefore able to minimize multicollinearity problems by regressing independent subsets of the training data to isolate the variables, as follows (see Table 3 for a comprehensive list of all conditions and frequencies used for each value).

1. We calculate background noise N_f as the mean power in each frequency over three nights with minimal discharge ($Q < 3$ L/s) and no precipitation or documented channel work. Only times from 9 P.M. to 3 A.M. are used in order to avoid stochastic noise spikes caused by human activities or channel work, which were independently removed during periods used for analysis (section 3). Other background anthropogenic noise such as traffic is negligible at this location due to the remote setting. N_f is then subtracted from P_f at all times to isolate the combined PSD of water turbulence, rainfall, and sediment transport.
2. We perform a least squares regression for the discharge coefficient a_f at each frequency during the subset of training times without rain or transport, such that equation (1) becomes simply

$$P_f\left(t_{p=q_s=0}\right) - N_f = a_f Q\left(t_{p=q_s=0}\right). \tag{2}$$

3. We select training times with rain present and discharge below a baseline flow of 50 L/s (implying $q_s = 0$), so that

$$P_f\left(t_{p>0,Q<50}\right) - N_f = a_f Q\left(t_{p>0,Q<50}\right) + b_f p\left(t_{p>0,Q<50}\right) \tag{3}$$

and solve for the coefficients for both precipitation (b_f) and discharge (a_f) through a multiple regression. Two points should be noted regarding this step: first, while the a_f from step (2) appear to be relatively accurate at higher discharge (Figures 3c and 3d), when transport is active, they tend to overestimate water-generated power at low discharge (most likely due to nonlinearity in the relationship between seismic power and discharge—see section 5.2.3). This leads to propagated error in the resulting rainfall coefficients if we simply use the a_f from step (2) to remove the predicted water turbulence spectrum and solve the remaining spectrum for b_f, which is why we instead perform an independent multiple regression. Second, it follows that, while the a_f determined here are more accurate for low discharge values (due to being characterized at $Q < 50$ L/s), they are less accurate during times with high discharge and active transport. To maximize the

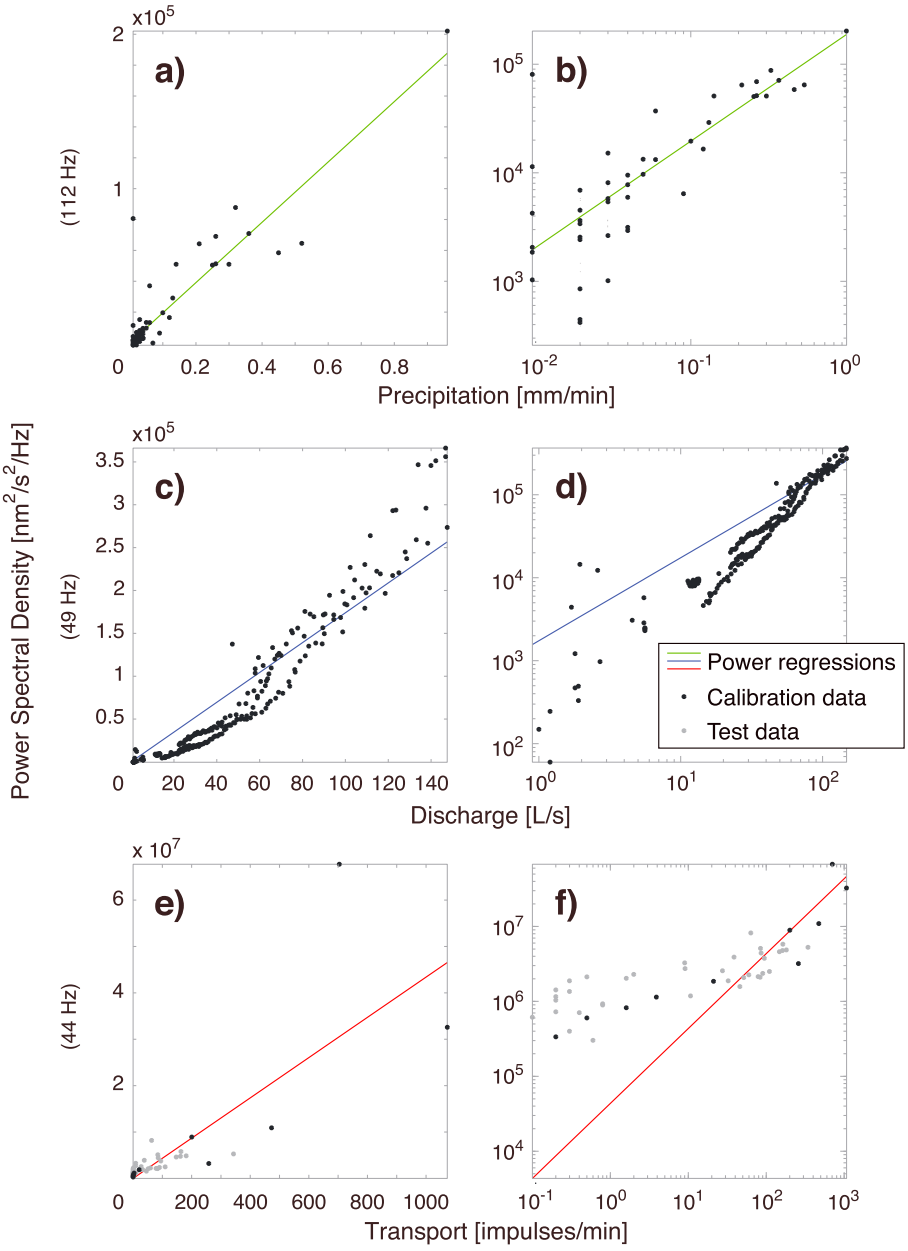

Figure 3. Isolated PSD associated with each variable at seismic station EB1, east-west component. Calibration data (black points) were used for regressions (colored lines), while test data (transport only—gray points) were only compared with predictions. PSD is shown for each variable's peak frequency (determined a posteriori, Figure 5) on (a, c, e) both linear and (b, d, f) log-log axes.

accuracy of our regression for transport at high discharges, our final step (4), below, therefore uses only the a_f calculated in step (2), along with the b_f calculated in step (3).

4. Lastly, we select the subset of training data during times with transport present (geophone counts > 0) and discharge above the transport threshold of 150 L/s. Using the precipitation and discharge data with coefficients a_f and b_f calibrated above, we can subtract out the predicted rain and discharge spectra from the observed PSD, so that equation (1) becomes

$$P_f\left(t_{q_s>0,Q>150}\right) - N_f - a_f Q\left(t_{q_s>0,Q>150}\right) - b_f p\left(t_{q_s>0,Q>150}\right) = c_f q_s\left(t_{q_s>0,Q>150}\right), \quad (4)$$

and a least squares regression yields the transport coefficients, c_f, at each frequency between 0 and 500 Hz.

3.3. Confidence Intervals and Covariance

Confidence intervals for each coefficient were calculated in two parts. First, individual error at each frequency (δa_f, δb_f, δc_f, henceforth denoted iteratively as $\delta\{i\}_f$, where $\{i\} = \{a,b,c\}$) was calculated separately for each fitted coefficient, using a standard covariance matrix estimation procedure for unknown measurement standard deviations [*Aster et al*., 2011]:

$$\delta\{i\}_f = \sqrt{s_{i,f}^2 \left(G_i^T G_i\right)^{-1}} t_{v,0.68}, \tag{5}$$

where G_i is the variable array (e.g., Q, p and/or q_s) used for each fit, and G_i^T is its transpose, so the inverse $(G^T G)^{-1}$ is the covariance matrix of the measured variables; due to our isolation procedures, in the cases of discharge and sediment transport this is simply the individual variance in each variable during its isolated regression period. The final variable, $t_{v,0.68}$, is the Student's t distribution value for v degrees of freedom and 68% confidence, so that $\delta\{i\}_f$ represents the 1σ confidence interval for each coefficient. It should be noted that, unlike cases in which the measurement standard deviations can be independently estimated, this empirical calculation of the covariance matrix (equation (5)) always results in an acceptable p test [*Aster et al*., 2011].

The estimated measurement standard deviation,

$$s_{i,f} = \sqrt{\frac{\sum \left(P_{i,f,\mathrm{obs}} - P_{i,f,\mathrm{model}}\right)^2}{v_i}}, \tag{6}$$

for each coefficient, i, is calculated at each frequency from the residuals between observed ($P_{i,f,\mathrm{obs}}$) and modeled ($P_{i,f,\mathrm{model}}$) PSD during the coefficient's isolated regression times. $v_i = N_i - m_i$ is the number of degrees of freedom for each fit, where N_i is the number of data samples and m_i is the number of independent variables being fitted ($m_{a,c} = 1$ for discharge and transport, $m_b = 2$ for precipitation).

The second stage of error calculation applies only to the transport coefficients c_f and accounts for the propagation of error from the predicted discharge and precipitation spectra during the transport regression (equation (4)). Assuming negligible error for both P_f and N_f, the error on the left hand side of equation (4) is $\pm(Q\delta a_f + p\delta b_f)$. The propagated error in the regressed transport coefficients, which we will denote Δc_f, is therefore

$$\Delta c_f = (Q\delta a_f + p\delta b_f)/q_s, \tag{7}$$

solved in the same least squares manner as equation (4). Combining equations (5) and (7), the coefficient values with 1σ confidence intervals are $a_f \pm \delta a_f$, $b_f \pm \delta b_f$, and $c_f \pm (\delta c_f + \Delta c_f)$.

It should be noted, however, that we are unable to account for all sources of error in this model, including any observational uncertainty in Q, p, q_s P_f, and stochastic noise spikes larger than our averaged N_f. Our uncertainty calculation also does not capture any model bias introduced by nonlinearity in the relationship between the seismic PSD and discharge or precipitation at rates higher than those allowed in our isolation procedure (e.g., $Q > 150$ L/s). Hence, the formal uncertainty estimates above may be considered statistical lower bounds on the parameter uncertainty.

Due to the isolation procedure we used, covariance among discharge, precipitation, and sediment transport data is not calculable through standard linear methods, as they do not overlap at any time. To calculate the covariance between the regression coefficients, we therefore used a bootstrap approach to resample the subset of data used for each regression to obtain an array (n = 1000) of bootstrapped values for each coefficient at each frequency. The normalized covariance (i.e., Pearson's correlation coefficient) between these bootstrapped coefficients is shown at each frequency from 0 to 500 Hz in supporting information Figure S1.

3.4. Predictive Sediment Transport Model

For any given time t, we now have data for the seismic PSD at each frequency band (P_f), water discharge (Q), and precipitation (p), as well as the regression coefficients a_f, b_f, and c_f calibrated above. Rearranging equation (1) thus provides a predictive equation for calculating the bed load sediment transport rate at time t, $q_{s,\mathrm{pred}}(t)$:

$$q_{s,\mathrm{pred}}(t) = [P_f(t) - a_f Q(t) - b_f p(t) - N_f]/c_f. \tag{8}$$

Since equation (8) yields a sediment transport prediction at each frequency, it was solved in the least squares sense to maximize prediction agreement among frequencies 16–100 Hz. This frequency band was selected because it is the range in which all regression coefficients are positive, and c_f indicates that power is being generated by sediment transport, as discussed in section 5.3.

Error margins ($\Delta q_{s,\mathrm{pred}}$) on the sediment transport predictions were calculated by propagating the error on each coefficient through equation (8)

$$\Delta q_{s,\mathrm{pred}}(t) = \left|q_{s,\mathrm{pred}}(t)\right| \frac{1}{n} \sum_{f=16}^{100} \left(\frac{\delta a_f Q(t) - \delta b_f p(t)}{P_f(t) - a_f Q(t) - b_f p(t) - N_f} + \frac{\delta c_f - \Delta c_f}{|c_f|} \right), \tag{9}$$

where n is the number of discrete frequencies used to solve equation (8) (16–100 Hz, in 1 Hz bands). The $1/n$ sum in equation (9) yields the mean relative error over n frequencies ($n = 85$). Again, this represents only a formal lower bound on the uncertainty in our sediment transport predictions.

Over the remaining installation period following the calibration storm in which a_f, b_f, and c_f were regressed, we use the precipitation, discharge, and seismic test data to calculate the predicted sediment transport values from equation (8), with the stipulation that predicted transport must be zero at times with $Q < 150$ L/s (the approximate transport threshold).

4. Results

4.1. Regressions

Figure 3 shows the linear regression between the seismic PSD and each variable (station EB1, east-west channel only) at its coefficient's peak frequency in both linear (Figures 3a, 3c, and 3e) and log-log (Figures 3b, 3d, and 3f) space, along with the isolated and corrected PSD used for each regression. The corrected PSD for water discharge is simply the PSD registered concurrently for each discharge datum. However, since precipitation and sediment transport do not occur in isolation, their corrected PSDs are those used for regression, calculated by subtracting the modeled power contributions of the other components (discharge and precipitation plus discharge, respectively). The corrected PSDs for transport and precipitation therefore contain any error propagated by this calculation. However, as the formal error represents only a lower limit on the true PSD uncertainty (see section 3.3) and is at most 9% the magnitude of the precipitation PSD and 2% the magnitude of the transport PSD, we have chosen to omit these potentially misleading error bars from Figure 3. Note that the range of values shown for discharge and precipitation is limited due to our isolation procedure; the PSD regressions are extrapolated to higher values when removing the theorized contributions of discharge and precipitation during transport events.

Figure 4 shows the discharge, precipitation, and transport data for the calibration storm on 18 July 2013, as well as the seismic spectrogram and the calculated isolated spectrogram components generated by each variable (i.e., $a_f Q$, $b_f p$, and $c_f q_s$ from equation (1)).

The least squares coefficients for water discharge (a), precipitation (b), and sediment transport (c) for each component (east-west, north-south, and vertical) and at each seismometer are shown in Figure 5 with the 1σ confidence margins calculated in section 3.3. Note that the discharge and transport coefficients are shown on a different vertical axis than the precipitation coefficients because they experience near-complete attenuation above 100 Hz (supporting information Figure S2). As mentioned in section 3.4, this attenuation motivated the use of only the 16–100 Hz band in calculating sediment transport predictions. The regression coefficients a_f, b_f, and c_f contain both the coupling between each variable's measured units (L/s, mm/min, and geophone impulses/min, respectively) and the seismic ground velocity generated at each respective source, as well as the attenuation of each seismic signal between the source and the seismometer (i.e., the Green's function). They also represent each process's spectral contribution to the signal at the seismometer or the power registered per frequency per unit discharge, precipitation, or transport.

The precipitation coefficients exhibit more variability between seismometers and between directional components than the discharge and bed load transport coefficients (Figure 5). In addition, the precipitation coefficients are more broadband (~16–480 Hz) than the discharge and bed load transport coefficients (~16–100 Hz), although they do eventually decline at higher frequencies (Figures 5a–5c). At the station nearest the river and least affected by attenuation, the discharge and transport coefficients both show

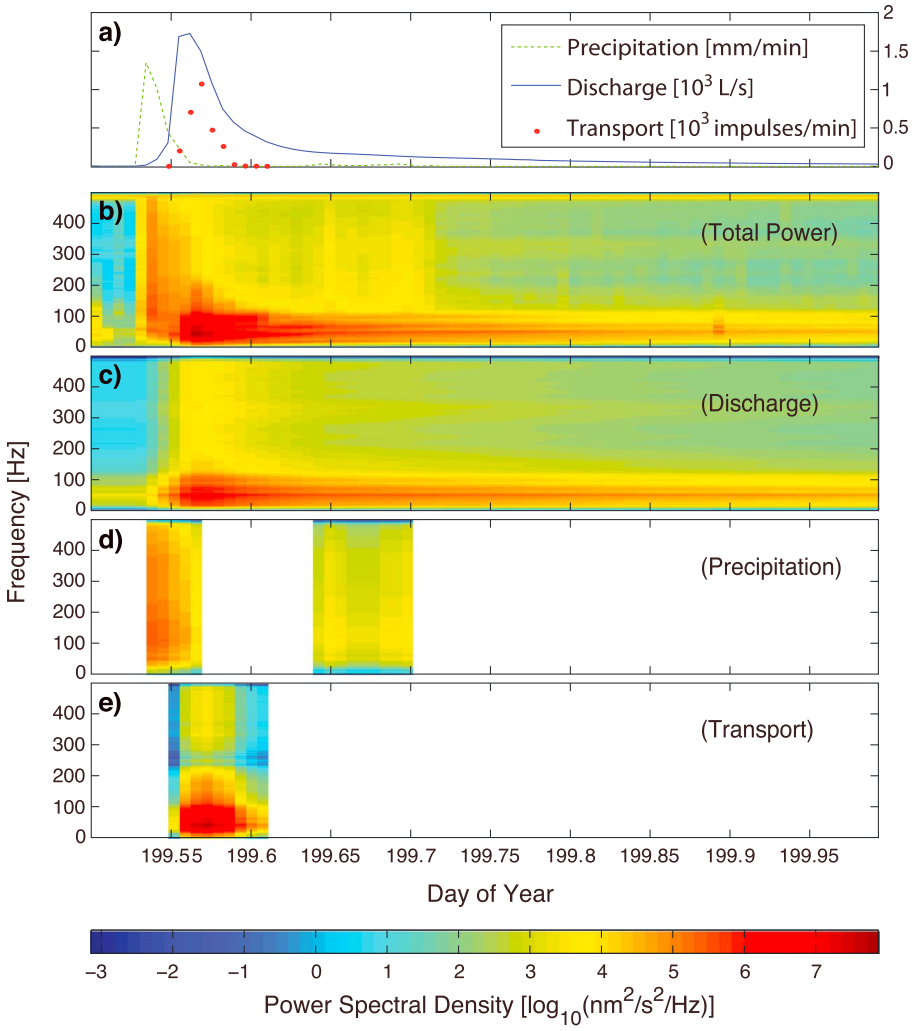

Figure 4. (a) Training data from a single storm on 18 July 2013 (Julian day 199), along with (b) the concurrent spectrogram of seismic power spectral density and isolated spectrogram components calculated for (c) discharge, (d) precipitation, and (e) bed load sediment transport.

two distinct peaks, although both peaks appear at very slightly higher frequencies for discharge than transport (49 Hz and 67 Hz, and 44 Hz and 62 Hz, respectively, at EB1 east-west channel). At the two farther seismometers, these peaks are less distinct, but maxima do appear consistently in roughly the same frequency range.

Figure 6a shows the observed rain, discharge, and transport data over the entire 2 month installation. The storm events in these data are visible in the spectrogram of observed seismic PSD at each frequency over the same time period (Figure 6b). The least squares model spectrogram in Figure 6c shows the power spectral density $P_f(t)$ calculated in equation (1), using the calibrated coefficients at each frequency and observed discharge, precipitation, and transport data at each time. This model spectrogram reproduces the major features of the observed seismic data, validating the viability of both the regression coefficients, a, b, and c, and the hypothesis that the seismic signal can be reconstructed with only these three parameters and discharge, precipitation, and transport data.

4.2. Sediment Transport Predictions

The sediment transport predictions made with equation (8) are shown in Figure 7, along with all observed discharge, rain, and transport data. Detailed figures for each of the five events with recorded transport can

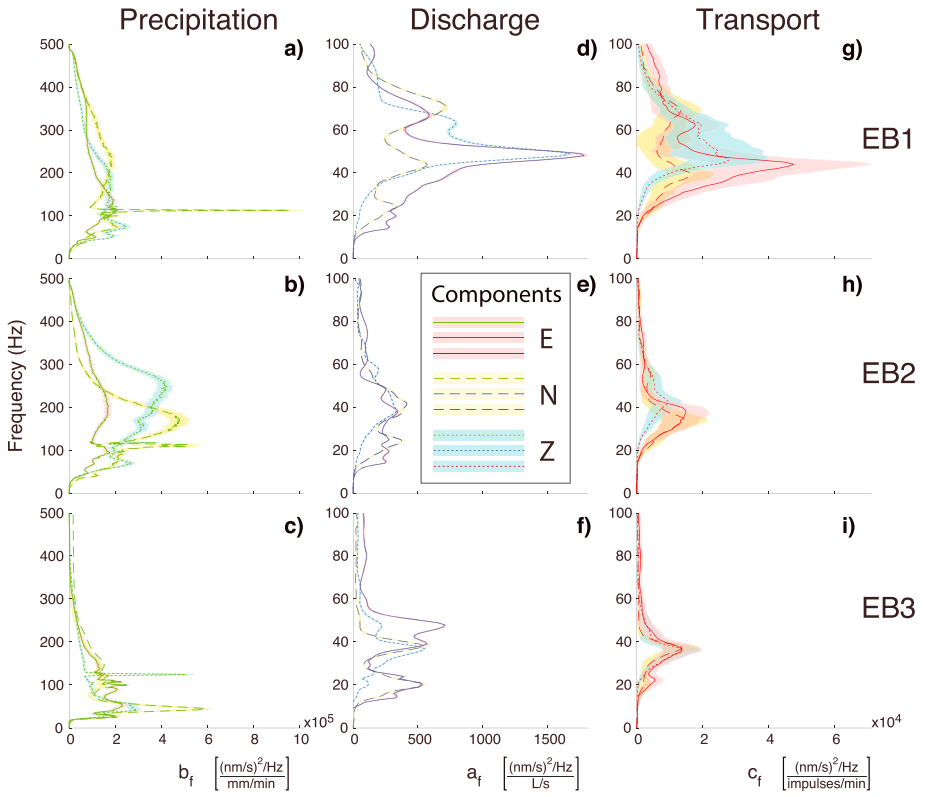

Figure 5. Regression coefficients and 1σ confidence intervals for each process (columns) at each seismometer (EB1–EB3, rows), for the east-west (E), north-south (*N*), and vertical (*Z*) components of ground motion. Coefficients represent both attenuation (Green's function) and the force coupling between each variable's measured units and seismic ground velocity. Note that while (a–c) precipitation coefficients are shown for 0–500 Hz, (d–f) discharge and (g–i) transport coefficients are shown only for 0–100 Hz, as they attenuate essentially to zero for higher frequencies (see supporting information Figure S2).

be seen in supporting information Figure S3. Calculated transport accurately shows nonzero values at all times when actual transport was occurring and is also nonzero for 2 times when the geophones did not register transport (days 220 and 221, or 8 and 9 August; Figure 7). These latter times occur during floods with peak flow discharges close to 300 L/s, the threshold for transport of particles large enough to trigger the geophones' recording threshold ($>$1 cm in diameter). Evidence discussed in section 5.1 suggests that transport of grains $<$ 1 cm occurred during these events, indicating that during these floods, the seismometers captured transport events too small for the geophones to register.

Sediment transport predictions (equation (8)) are plotted against measured geophone impulse counts in Figure 8 ($r^2 \sim 0.6$, $p < 10^{-10}$). The sediment transport data and predictions are shown in terms of both geophone impulse counts (impulses/min) and mass flux (kg/min). Mass flux was calculated using the calibration relationship $M = \mathrm{IP}/3.27$, where M and IP are, respectively, the mass flux of bed load sediment and the number of geophone impulses generated by grains with $D > 9.5$ mm [*Rickenmann et al.*, 2012]. Our model appears to overpredict sediment transport at low rates but converges with observations for higher transport rates, which are arguably more important in evaluating volumetric erosion rates. As discussed in section 5.1, however, at least some of the apparent overprediction at low rates also reflects the ability of the seismometers to capture the impacts of grains $<$ 1 cm in diameter, which are not recorded by the geophones.

5. Discussion

5.1. Sediment Transport Predictions

As seen in Figure 8, the predicted sediment transport deviates from indirect geophone measurements significantly at low transport (~10^2 impulses/min). We suggest three possible explanations for this discrepancy: first, there could be higher covariance between water discharge and sediment transport at lower discharge,

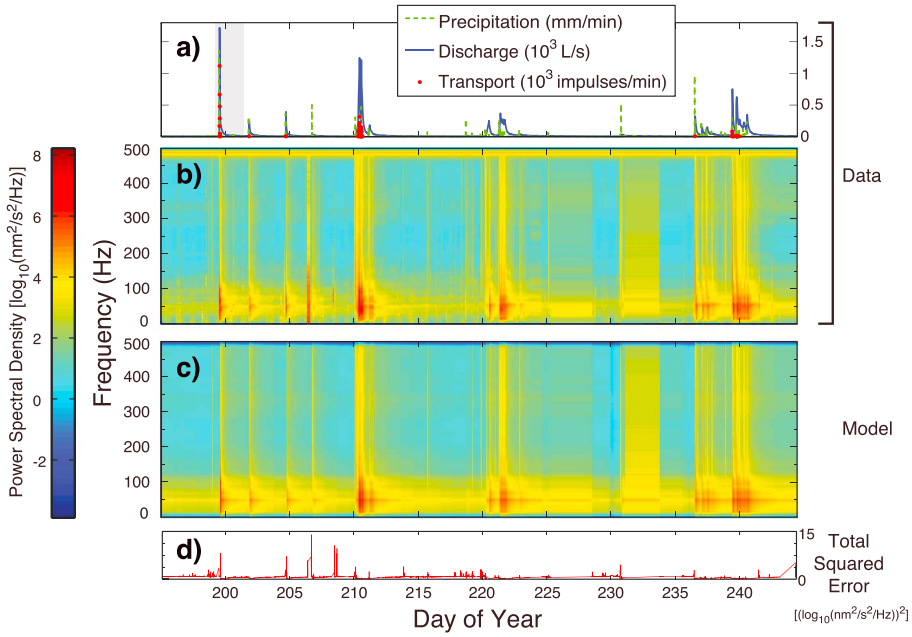

Figure 6. Model results validate coefficients and methodology. (a) Observed precipitation, water discharge, and bed load transport (geophone) data over entire installation, with calibration storm indicated by gray bar. (b) Observed seismic power spectral density over the same time period, showing the signals recorded during each storm event. (c) Power spectral density predicted by our least squares model at each frequency, with (d) total squared error shown over time.

causing the discharge signal to map onto the transport coefficients and increasing error at lower fluxes. This explanation is unlikely because sediment transport is a thresholded process, so we would expect to see higher covariance at higher transport rates and less covariance at lower discharges when stage can vary more without inducing notable transport. Second, because we calibrated the coefficients for transport with the largest storm event (and thus the highest available transport rates), nonlinearity between sediment transport and seismic power could skew the regression such that our optimization is biased toward higher fluxes

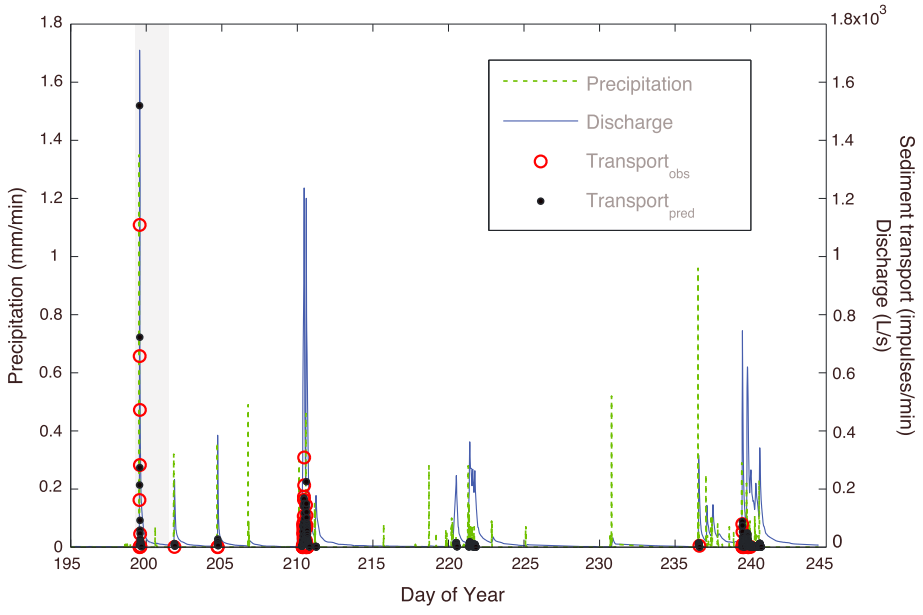

Figure 7. Predicted bed load sediment transport plotted with all observed data for precipitation, discharge, and sediment transport (geophone impulses) throughout the installation.

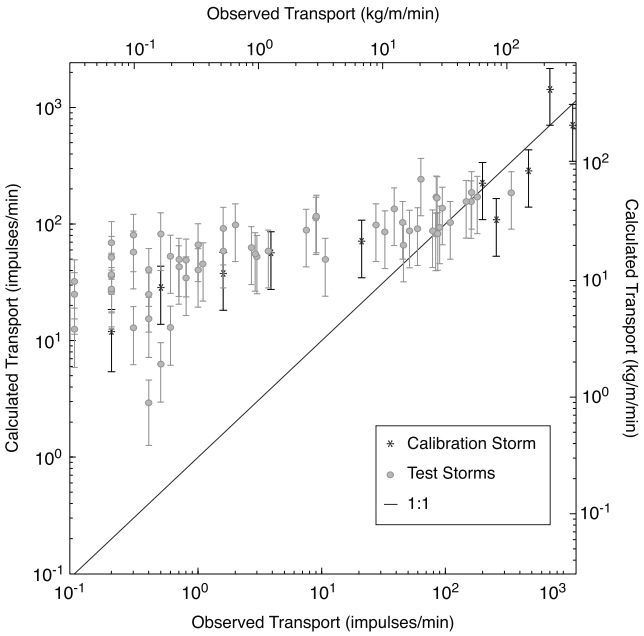

Figure 8. Predicted bed load sediment transport compared to geophone observations for calibration (black) and test (gray) storms. Transport rates shown as both geophone impulse counts (impulses/min) and mass flux (kg/m/min) calculated using the calibration relation for $D > 9.5$ mm. $r^2 \sim 0.6$, $p < 10^{-10}$.

and less accurate for lower fluxes. We discuss our assumption of linearity between seismic power and sediment transport in section 5.2.1, below, and find it reasonable over the frequencies and grain sizes observed.

Finally, particles small enough ($D < 1$ cm) to be neglected by the geophone recording software are registered by the seismometers and add enough to the seismic signal to significantly affect the PSD at lower transport rates, when small grains make up fractionally more of the transport signal. To better demonstrate this, note that q_s does not represent the true sediment flux, but the number of impulses recorded on the geophones (empirically found to scale linearly with the mass flux of particles larger than 1 cm in diameter). We can instead represent the true mass flux of sediment as some function of $q_s + q_o$, where q_o is an offset produced by the undetected flux of grains smaller than 1 cm in diameter. Since the seismic power is generated by the full sediment flux, i.e., $P = P(q_s + q_o)$, plotting P against q_s produces a curved line in log-log space, as we see in Figure 3f. Due to this unaddressed offset, our regressions with seismic power underestimate the true power at low transport rates when the offset generates proportionately more of the total power than at high transport rates. This, in turn, leads to an overestimation of geophone impulses at low seismic power (i.e., equation (8) is missing the $-q_o$ term). The subsequent overestimation of geophone impulses at low transport rates is therefore at least partially due to the additional transport of small grains that are not recorded by the geophones but are registered by the seismometers. Hence, the data introduce the exciting possibility that our seismic model may be more accurate at measuring sediment transport rates when the channel conditions are near the threshold for motion.

To test the above premise, we performed a secondary regression to solve for the hypothetical offset value by substituting $q_s + q_o$ for q_s in equation (4). Note that this regression assumes a constant q_o; in fact, q_o is equal to zero below the discharge threshold required to move the smallest grains present and scales with discharge above that threshold. Supporting information Figure S4 shows the amended PSD regression with a constant offset taken into account. This regression yields a unique value for q_o at each frequency (supporting information Figure S5). We used the mean of these values, $q_o \sim 28$ impulses/min, between 20 and 80 Hz, the range in which they appear roughly constant, and the sediment transport coefficients contain significant power. This approach does not noticeably alter the calculated values of c_f. We then recalculated our sediment transport prediction, substituting $q_{s,\mathrm{pred}} + q_o$ for $q_{s,\mathrm{pred}}$ in equation (8) so that the final $q_{s,\mathrm{pred}}$ is calculated by subtracting q_o (Figure 9). The offset regression (supporting information Figure S4) demonstrates the curvature exhibited by the data but does not precisely fit the observations, leading to an overestimation of seismic power at low transport rates. We expect that this mismatch is because q_o is not a constant, but instead varies with discharge (and therefore with the observed transport rate q_s). Thus, the recalculated sediment transport predictions ($r^2 \sim 0.65$, $p < 10^{-7}$) shown in Figure 9 correct much of the offset at low transport rates, but not all of it, again likely due to unaccounted variation in q_o.

While this calibration is relevant for bed load transport measurements made using geophone plate or hydroacoustic systems, it is unlikely to be necessary for many methods that do not involve a grain size threshold, such as sediment traps. However, our results indicate that at low transport rates, the relationship between

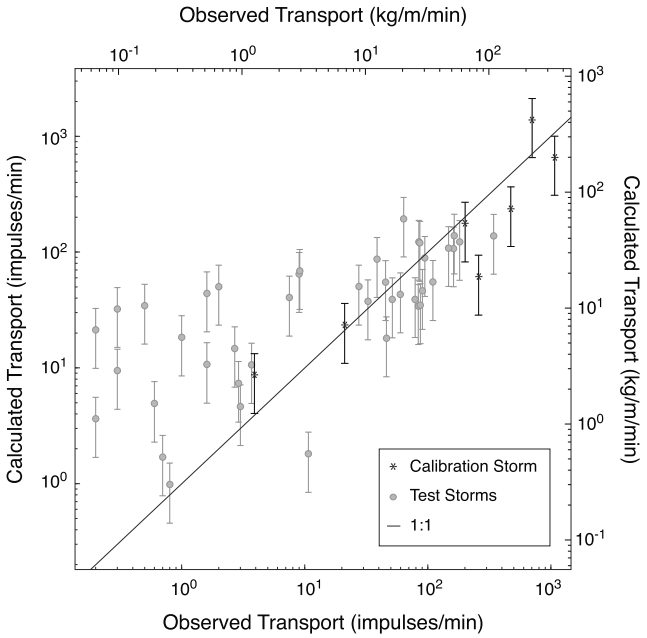

Figure 9. Recalculated predicted bed load transport rates with calculated hypothetical transport offset q_o, compared to geophone observations for calibration (black) and test (gray) storms. Transport rates shown as both geophone impulse counts (impulses/min) and mass flux (kg/m/min) calculated using the calibration relation for $D > 9.5$ mm. $r^2 \sim 0.65$, $p < 10^{-7}$.

transport and seismic power is particularly nonlinear. Hence, regardless of their measurement techniques, future models may improve their accuracy at low transport rates by addressing this nonlinearity, possibly through examining variation in q_o with discharge, and including the threshold of incipient sediment transport.

The existence of an offset q_o is also supported by low-voltage data from the geophones, which independently log impulses between the geophones' primary recording threshold and a lower voltage noise threshold [*Wyss et al.*, 2014, 2016]. While we were unable to quantitatively utilize the low-voltage data recorded during our study period due to a lack of calibration, they do serve as a qualitative indicator of the presence or absence of transport of particles <1 cm. During all storms observed, the low-voltage impulse count is nonzero, indicating the presence of small particle transport and corroborating the presence of the offset effect (q_o) proposed above. Further, during all three of the small storms (days 220, 221, and 236) in which the model predicted transport that was not observed by the geophones (Figure 7), the low-voltage data also indicate the presence of small particle transport.

Supporting information Figure S6 shows the number of impulses recorded between the lower noise threshold of 0.056 V and an upper threshold of 0.112 V (low-voltage data) plotted as a function of those recorded above a threshold of 0.112 V (high-voltage data) for three transport events (days 199, 210, and 239 combined) during the observation period. These high-voltage data are essentially the same as the transport intensities used elsewhere in this paper. These data further support the presence of the hypothesized offset effect in two ways. First, at times when the geophones register low or no transport (small or zero high-voltage impulse rates), we find nonzero low-voltage impulse rates. Second, we observe a distinct decrease in the slope of the data for high-voltage impulse rates above ~10 impulses/min (supporting information Figure S6), roughly the same point at which our seismometer predictions and the geophone data begin to converge (Figure 8). For high-voltage impulse rates lower than 10 impulses/min, a linear regression of the data yields a slope of 4.2, while larger high-voltage impulse rates regress with a slope of 2.6. This indicates that the ratio of small grain transport to large grain transport is higher at low transport rates (below ~10 impulses/min).

At higher transport rates (above ~10 impulses/min), the transport of small grains remains roughly proportional (linear) to that of grains >1 cm, supporting our previous interpretation that q_o scales with q_s. However, energy delivery to the bed is strongly dominated by the largest grains [*Tsai et al.*, 2012; *Turowski et al.*, 2015]; therefore, as transport rates increase and larger grains are entrained, they generate proportionally more of the signal. As the transport rate surpasses ~10 impulses/min, it appears that the signal of small grain transport is effectively drowned out by the transport of larger grains.

5.2. Is a Linear Approximation Valid?

In using a linear regression model, we have explicitly assumed a roughly linear relationship between each variable (discharge, precipitation, and transport) and the seismic power it generates. Here we discuss the physical justifications for and possible errors entailed in such an assumption.

5.2.1. Sediment Transport

The amplitude of seismic ground displacement is linearly proportional to the impact force generating the signal [*Aki and Richards*, 2002]. Transforming from displacement amplitude to the power spectral density (PSD) of ground velocity maintains this linearity, since power scales as the square of the seismic amplitude, while velocity is the derivative of displacement. Hence, under the simplifying assumption that all particles travel via saltation [e.g., *Hsu et al*., 2011], the PSD of seismic ground velocity generated by a characteristic grain size in motion will scale linearly with the rate of impacts, which in turn scales linearly with total bed load flux [*Tsai et al*., 2012].

This reasoning, however, does not take into account changes in the mobile grain size distribution, which we expect to strongly influence the amount of energy delivered to the channel bed [*Turowski et al*., 2015]. Below we discuss two possible effects of grain size evolution on the seismic signal. First, we address a theorized shifting of the impact spectrum's frequency content with changing grain size, which we demonstrate to be inconsequential here. Second, we find that dependence of the PSD on grain size does not affect the transport signal within the range captured in this study; at our recorded transport rates, a linear approximation does appear to be reasonable, although the lower end of the signal is dominated by the effects discussed in section 5.1.

5.2.1.1. Frequency Dependence on Grain Size

According to Hertzian impact theory [*Hunter*, 1957], the dominant frequency excited upon impact is expected to scale inversely with grain size. This principle has also been observed by *Huang et al*. [2007], who examined the seismic signals generated upon dropping rocks of different sizes and found that larger rocks produced ground motion with lower peak frequencies. As river shear stress and bed load transport rates increase, we therefore expect the seismic spectrum to shift to lower frequencies, reflecting the entrainment of larger grains, as follows.

The time-dependent impulsive force $F(t)$ exerted by a particle upon the channel bed can be modeled as a classic Hertzian "half-sine" impact [*Hunter*, 1957]:

$$F(t) = A\sin(\pi t/t_c), \quad 0 \le |t| \le t_c, \tag{10}$$

where A is the amplitude of the impulse force, t is time, and t_c is the time of contact between the particle and its bed.

Assuming the channel bed and bed load are composed of the same material and thus have the same material properties, the frequency f of the Hertzian impulse force is [*McLaskey and Glaser*, 2010; *Thorne*, 2014]

$$f = 1/2t_c = 0.47(\rho_s\delta_s)^{-2/5}\frac{w^{1/5}}{R_s}, \tag{11}$$

where w is the velocity at which the particle of sediment impacts the bed, R_s is the particle's radius, $\delta_s = (1 - \nu_s{}^2)/(\pi E_s)$, and ρ_s, ν_s and E_s are the density, Poisson's ratio, and Young's modulus, respectively, of the bed and bed load sediment material. Note that this model applies specifically to saltating grains; the deviation caused by rolling and sliding transport modes remains relatively unstudied and hence is not discussed here.

Assuming the particle reaches its terminal settling velocity before impacting the bed [e.g., *Hsu et al*., 2011], its speed upon impact is [*Lamb et al*., 2008]

$$w = \left(\frac{8R_b g R_s}{3C_d}\right)^{1/2}, \tag{12}$$

where $R_b = (\rho_s/\rho_w) - 1$ is the particle's buoyant density and C_d is the particle's drag coefficient. We also performed the following analysis under the assumption that the particle does not have time to reach terminal velocity before impact and instead impacts the bed with a velocity of roughly twice the mean theoretical particle descent speed [*Sklar and Dietrich*, 2004]; the results of this calculation do not differ significantly from the terminal settling velocity results and are therefore not shown.

Since empirical studies show that the geophone impulses scale linearly with mass flux over the geophones [*Rickenmann et al*., 2012], we scale equation (12) with grain mass instead of radius. Approximating grains as spherical, substitution into equation (11) thus yields the theoretical frequency peak of the impulse force generated due to bed load saltation of a grain of mass M_s

$$f = 0.08\left(\frac{R_b g}{C_d \rho_s \delta_s^4}\right)^{1/10} M_s^{-3/10}. \tag{13}$$

Supporting information Figure S7 shows the predicted peak frequency as a function of grain size and mass, using typical values for the Erlenbach and mudstone: $\rho_s = 2750$ kg/m^3, $E_s = 3 \times 10^9$ Pa, $\nu_s = 0.2$, $g = 9.81$ m/s^2, and $C_d \sim 1.4$ (empirical drag coefficient for natural grains under turbulent flow; [*Fredse and Deigaard*, 1992]). The peak frequency of the impact force is highly nonlinear with impactor mass (supporting information Figure S7 and equation (13)). However, all peak frequencies excited by impactors of the relevant size range (i.e., ~1–30 cm) in the Erlenbach are almost completely attenuated by the time they reach the seismometers (Figure 6), and most are also far above the monitored frequency range (supporting information Figure S7). We therefore assume that the signal's frequency-dependent variation with active grain size is negligible within the observable frequencies.

This assumption is similar to the simplification used in the theoretical model for transport-generated seismic signals developed by *Tsai et al*. [2012], who neglected the seismic frequency dependence on grain size by modeling a particle's impulsive force as instantaneous (i.e., $F(t) \propto \delta(t)$, where $\delta(t)$ is the Dirac delta function). Our results also support the subsequent implication that the peak frequency of the seismic signal is predominantly controlled by the station-receiver distance, rather than by grain size [*Tsai et al*., 2012]. These findings are especially relevant given the near-complete attenuation of the theorized peak frequencies in spite of our seismometers' extreme proximity to the channel; however, further research may find this assumption to be less valid in more slowly attenuating substrates (i.e., bedrock channels).

5.2.1.2. Amplitude Dependence on Grain Size

Tsai et al. [2012] found that a bed load flux, $q_s(D)$, of particles of a given size D will generate a PSD $P_f(D)$ that scales as $P_f(D) \propto D^3 q_s(D)$. The total measured PSD used for the least squares regression is integrated over the grain size distribution, $P_f = \int_D P_f(D) dD$. However, *Tsai et al*. [2012] also note that the spectral signal appears to be dominated by largest grain size, D_{94}. This finding is further supported by *Turowski et al*. [2015], who used the Erlenbach's in-stream geophones to examine the energy delivered to the channel bed and found that energy delivery is dominated by larger grains. Therefore, to simply examine the trend in seismic power with changes in grain size, we will assume that the total PSD scales with the 94th percentile grain size and some fraction of the total sediment flux as $P_f \propto {D_{94}}^3 q_s$. Both the mobile grain size distribution and sediment flux will covary with discharge, so that D_{94} scales as some function of q_s (i.e., $D_{94} \propto {q_s}^{\alpha}$), where α is some value > 0. We can thus restate the seismic power scaling argument as $P_f \propto {q_s}^{\alpha+1}$. Since sediment flux is raised to some unknown exponent that must be greater than 1, we expect that the PSD plots against sediment transport at a slope greater than 1 on log-log axes. However, *Turowski et al*. [2013] found that energy delivered to the bed of the Erlenbach by bed load transport scaled nearly linearly with bed load transport rates, implying that, at least for some storms at this field site, α may be quite small.

In Figure 3f, we see that the PSD at the highest transport rates appears to converge on a slope close to 1 (lower transport rates plot at a slope <1 for reasons unrelated to linearity; see discussion in section 5.1). Theoretically, it is likely that this relationship converges on a slope >1 at higher transport rates, but the range of transport rates we are able to observe here is dominated by the offset effect caused by small grains at low transport.

5.2.2. Rainfall

Assuming raindrop size does not change over the course of a storm, and that drops achieve terminal velocity before reaching the ground, then the seismic power generated by rainfall should simply equal the power generated by a single raindrop impact multiplied by the number of drops impacting. While raindrop size, in fact, increases with rainfall rate [*Pruppacher and Klett*, 1997], the interception of raindrops by dense but spatially inhomogeneous forest canopy above the seismometers strongly influences both drop size and velocity by the time rainfall reaches the ground. We therefore assume that the dependence of raindrop size on rainfall rate is relatively small compared to the scatter due to canopy interception, and that seismic power will scale approximately linearly with rainfall rate. Examination of Figure 3 reveals that, while the signal of rainfall demonstrates significant scatter as expected, the linear assumption used is reasonable.

5.2.3. Water Turbulence

We assume that the seismic power generated by water turbulence scales linearly with stream power or the rate at which stream potential energy is converted to work done on the river bed per unit bed area (i.e., the power delivered to the bed by water turbulence). The well-known equation for specific stream power Ω is [*Bagnold*, 1966]:

$$\Omega = \rho_w g Q S / W, \tag{14}$$

where S is the channel slope, and W is channel width. As the channel cross section is roughly rectangular, we assume that W remains roughly constant once discharge is high enough to cover the bed; this assumption does not address nonlinearity introduced by changing the active channel width below that threshold, which we assume to be negligible. Since equation (14) is therefore approximately linear with discharge Q, it follows that the rate of seismic power can also be approximated as linear with discharge [e.g., *Hsu et al*., 2011; *Burtin et al*., 2008].

This approximation is further supported by *Gimbert et al*. [2014], whose theoretical model for the seismic signal generated by turbulent flow in rivers predicts that the PSD of ground velocity will scale with flow depth (h) as $P_f \propto h^{7/3}$. Using the rating curve empirically calibrated between discharge and stage at the Erlenbach (from which the discharge values used in this study were calculated), flow depth scales roughly as $h \propto Q^{1/2}$ [e.g., *Nitsche et al*., 2012]; seismic power thus scales with discharge roughly linearly ($P_f \propto Q^{7/6}$).

Figures 3c and 3d demonstrate a slightly nonlinear trend between seismic power and discharge below 150 L/s (the approximate sediment transport threshold); this nonlinearity may lead us to overestimate the seismic power generated by water turbulence at low discharges while underestimating it at high discharges. A nonlinear regression on discharge values $<$150 L/s yields a best fit relationship of $P_f \propto Q^{1.6}$. However, running our full model using either $Q^{1.6}$ or $Q^{7/6}$ (above) decreases the accuracy of our final sediment transport predictions (both yield $r^2 \sim 0.5$, compared to $r^2 \sim 0.6$ for the linear fit), implying that the discharge-PSD relationship may actually be better represented over the full range of discharge by our linear assumption.

5.3. Coefficients and Dominant Frequencies

Figures 10a and 10b shows the coefficients for water discharge, a_f, with the average spectrum (E-W component, station EB1) during all times with discharge between 140 L/s and 150 L/s (the bed load transport threshold); the averaged spectrum is normalized by discharge rate to match the coefficient units of seismic power per unit discharge. Similarly, Figures 10c and 10d show the rainfall coefficients b_f along with the averaged, precipitation-normalized spectrum during three representative times with high rainfall (0.36–0.96 mm/min). Figure 10 thus corroborates our calculated regression coefficients, assuming these averaged, normalized spectra are roughly representative of the isolated spectral signals of river discharge and rainfall.

While, to our knowledge, the isolated spectra generated by water discharge, rainfall, and bed load transport have never been identified definitively, several prior studies have distinguished components and frequency bands that appear to be associated with these processes. *Tsai et al*. [2012] assumed that the dominant waves generated by vertically impacting bed load saltation would be Rayleigh waves, therefore making the vertical component of ground motion larger than either horizontal component. Other studies have both supported [e.g., *Roth et al*., 2014] and questioned [e.g., *Schmandt et al*., 2013; *Burtin et al*., 2010] the validity of this assumption. *Gimbert et al*. [2014] theorized that water turbulence would generate a combination of Rayleigh and Love waves, resulting in ground motion in the 1–100 Hz frequency band in both vertical and horizontal components. *Burtin et al*. [2011] analyzed the vertical component of seismic data from a river in the French Alps (minimum source-receiver distance ~15 m) and observed a peak in the 60–90 Hz band during rain storms, which they suggest could be generated by raindrop impacts. They also found that the linear correlation between water depth and seismic energy was highest in the 3–9 Hz frequency band, but decreased with increasing frequency and was very poor above 40 Hz. Conversely, while they were unable to identify a distinct frequency band with a well-constrained linear relationship to bed load transport, the correlation with bed load flux did appear to improve with increasing frequency between 15 and 40 Hz. This implies that water and bed load may occupy distinct spectral spaces. *Schmandt et al*. [2013] examined the signal of bed load sediment transport in the Grand Canyon (source-receiver distance ~35 m) and concluded that bed load transport was the dominant seismic source for 15–45 Hz, while fluid processes were found to generate signals at 0.73 Hz and 6–7 Hz. On a small stream in Luxembourg (source-receiver distance ~2 m), *Barrière et al*. [2015] found that the vertical component of seismic PSD peaked at 30–35 Hz during a time with isolated water discharge. Combined water discharge and sediment transport was observed to generate power between 10 and 70 Hz, with a peak at 30–40 Hz. They further found that the combined discharge and transport peak in the horizontal component of the PSD was both higher in magnitude and shifted to lower frequency content by ~10 Hz. They attributed this shift to reflect a stronger turbulent flow-induced signal generating lower frequency power in the horizontal component.

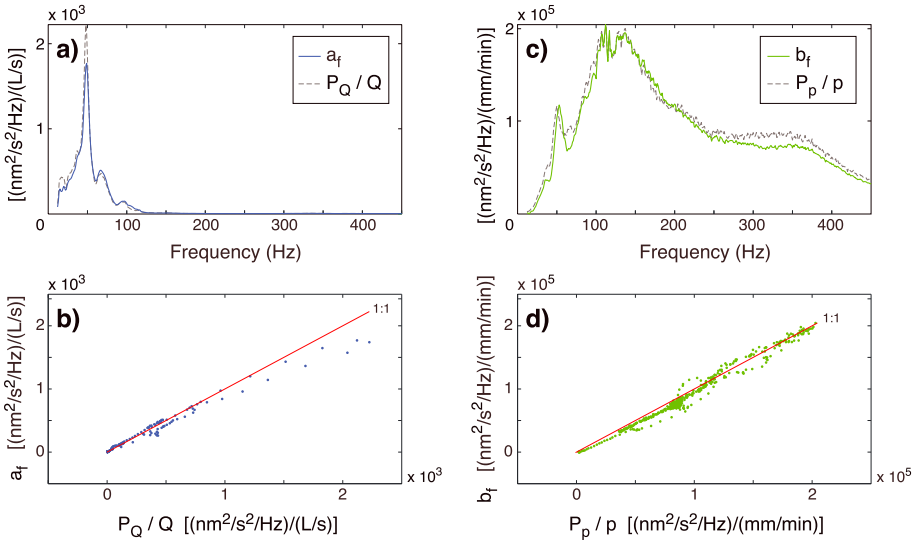

Figure 10. Regression coefficients for water discharge (a_f) and precipitation (b_f) compared with the normalized average seismic power spectral density (P_Q/Q and P_p/p) during times dominated by water discharge (Q) or precipitation (p), respectively. Normalized spectra and coefficients are shown as a (a, c) function of frequency and in (b, d) direct comparison with the 1-to-1 line indicated in red. All data shown are from the east-west component of the signal at EB1.

In our data, the horizontal channel-parallel (east-west) coefficients for both discharge and bed load transport are largest at EB1, the seismometer closest to the channel (Figure 5g); however, the coefficients of all three components are comparable for the two farther seismometers (Figures 5h and 5i). This discrepancy may be due to site-specific resonances or scattering of the wave field in the alluvium. A strong horizontal component of bed load transport-generated ground motion parallel to the channel might suggest the dominance of horizontal Love waves generated by particles rolling or sliding along the bed [e.g., *Schmandt et al.*, 2013]. Horizontal channel-parallel motion could also be generated by particles impacting the bed at angles that are far from normal to the bed. We expect the former to be especially likely here, since the bed of the Erlenbach is composed of highly variable mixed grain sizes, with many protruding meter-sized boulders. If saltating particles frequently impact the upstream sides of these boulders, this would transmit predominantly horizontal forces on the bed, as we see at station EB1 (Figure 5g).

Our precipitation coefficients extend into higher frequencies than either discharge or bed load, like those of *Burtin et al.* [2011]. Our results correspond roughly to previous findings [e.g., *Schmandt et al.*, 2013; *Barrière et al.*, 2015] for the frequency range generated by bed load transport (Figures 5g–5i). However, we also find that the seismic power generated by water discharge peaks is slightly higher in frequency and largely overlapping with the transport peak. This may be due to a much smaller source-receiver distance at our site, compared with some previous studies [e.g., *Burtin et al.*, 2011; *Schmandt et al.*, 2013], or to site-specific factors such as the downstream waterfalls (~20 and ~60 m away), upstream tributary junction (~20 m away), or local streambed configuration.

At EB1, closest to the channel and least affected by attenuation, the spectra peak at 44–49 Hz for water discharge and 44–46 Hz for bed load sediment transport, depending on the signal component (Table 4). Both discharge and bed load transport generate ground motion with spectral power concentrated between ~16 and ~100 Hz (attenuating by ~60 Hz at the farther seismometers). Note, however, that the lower limit of this frequency range (16 Hz) is determined by the fact that a number of the 1–15 Hz coefficients exhibit negative values (see supporting information Figure S8). As negative coefficients would imply a decrease in seismic power with increasing activity and are thus

Table 4. Sediment Transport Coefficient Spectral Peaks at Each Seismometer and Directional Component (Hz)

	EB1	EB2	EB3
E	44	38	36
N	40	34	37
Z	46	43	36

physically implausible, this frequency range was deemed unreliable for analysis. These negative values may occur due to increased covariance among sediment transport, rainfall, and/or water discharge, implying that perhaps more than one of these processes does generate power in these frequencies. Regardless of sign, however, the amplitudes of all three coefficients between 1 and 15 Hz are negligible compared with their higher-frequency peaks (supporting information Figure S8).

We suspect that the concentration of the bed load signal below 100 Hz may be due largely to attenuation of higher frequencies, rather than its intrinsic spectral properties (see the discussion in section 5.2.1.1). However, the presence of a smaller secondary peak in the spectra around 60–71 Hz (Figures 5d and 5g) indicates that the primary, lower frequency peaks discussed above are caused by actual spectral structure, rather than attenuation effects.

5.4. Insight into Signal Sources From Attenuation

We infer that the precipitation coefficients (b) are broadband over ~16–480 Hz (Figure 5) because rain impacts directly above the seismometers and therefore does not attenuate significantly, while transport and discharge attenuate from the river source and thereby lose power from the higher frequencies. In part due to this attenuation, the discharge and transport coefficients occupy very similar frequency bands and do not appear easily separable. However, we can gain some insight into the signals' respective sources through the relative attenuation of the signals with distance, as demonstrated by their coefficients calculated at each seismometer.

Both the discharge and transport coefficients are highest at seismometer EB1 (Figure 5d, 5g, and 11b–11c), since it is closest to the river. However, while the transport coefficients decrease as expected between EB1, EB2 and EB3, the discharge coefficients do not and are actually higher at EB3 than at EB2 (Figures 5e, 5f, and 11b). Due to the seismometers being aligned at a slight angle to the channel (Figure 1c), points farther than ~14 m downstream (along-river distance) are actually closer to EB3 than EB2 (Figure 11d). This inversion in discharge coefficients therefore implies that the water discharge signal is predominantly sourced from $>$14 m downstream and is most likely primarily generated by one of two downstream waterfalls: a smaller waterfall near the discharge gauge (~20 m downstream) or a larger waterfall that marks the transition between the cement bed and the retention basin (~60 m downstream) (Figure 1c). This finding suggests that the seismic signal generated by water turbulence may be dominated by nonlocal sources in locations with features such as rapids or waterfalls. Such features should be taken into account both when selecting field sites and considering spectral decomposition of signals in seismic bed load monitoring studies.

The transport coefficients decay with distance between EB1, EB2, and EB3 (Figure 11c), consistent with what we would expect assuming roughly uniform transport along the channel reach, such that the transport signal is predominantly caused by bed load impacting the channel bed nearest the seismometers. The precipitation coefficients show no pattern of decay with distance (Figure 11a) and appear to vary only due to site-specific effects, corroborating our earlier theory that the signal generated by rainfall is dominated by raindrop impacts immediately proximal to the seismometers.

5.5. Attenuation

By approximating the frequencies at which significant attenuation occurs in the regression coefficients, we can obtain some rough constraints on the seismic attenuation or quality factor Q (not to be confused with discharge), which describes the fractional loss of seismic energy per oscillation. Since seismic waves attenuate exponentially as a function of frequency and travel distance, the seismic amplitude at a given source-receiver distance will be attenuated by a factor of e or more for frequencies above some e-folding frequency, f_e. Following the theoretical Green's function and velocities for Rayleigh waves used by *Tsai et al.* [2012], we expect e-folding attenuation to occur at $1 = \pi f_e r / v_u Q$, where r is the source-receiver distance and $v_u = 945.35(f_e/f_0)^{-0.374}$ is the seismic group wave velocity [*Tsai et al.*, 2012], with $f_0 = 1$ Hz, and Q is again the seismic quality factor. Because the seismic sources are spatially integrated (ie, discharge and transport are sourced from infinite points along the river), it is challenging to define an accurate seismic source-to-receiver distance r. Any quantitative estimate of seismic attenuation is therefore highly uncertain. However, using the vertical component of the sediment transport coefficient spectrum, c_f (Figures 5g–5i), a Q value of 5 yields reasonable e-folding frequencies of 76 Hz (EB1, $r \sim 4$ m), 56 Hz (EB2, $r \sim 6$ m), and 50 Hz (EB3, $r \sim 7$ m). This is well below the value of 20 assumed by *Tsai et al.* [2012], but very similar to the estimate of *Schmandt et al.*

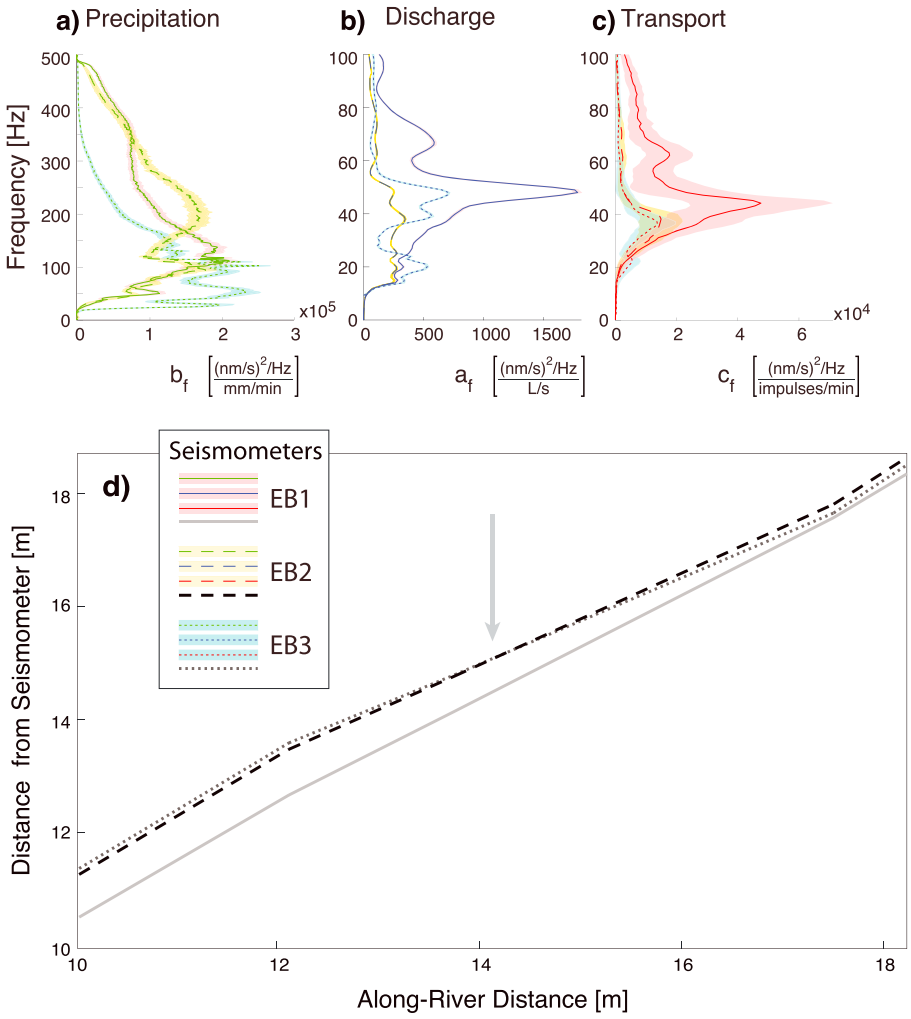

Figure 11. Regression coefficients for (a) precipitation, (b) discharge, and (c) transport for east-west channel only, replotted for comparison between seismometers. (d) Distance from each seismometer as a function of along-river downstream distance from the thalweg nearest the seismometers. EB3 is closer to the river than EB2 for positions ≳14 m downstream of the seismometers (gray arrow indicates approximate inversion point).

[2013], who found that $Q = 8$ produced agreement between observed and predicted sediment transport spectra on the Colorado River, although they note that this estimate may have been too high. On the other hand, a similar estimate using the discharge coefficient spectrum, a_f, (Figures 5d–5f) and the approximate distance to the nearest waterfall ($r \sim 21$ m) requires Q values closer to 20 for reasonable f_e frequencies between 60 and 70 Hz. This may reflect the large variation in attenuation between different paths. However, our estimated r and f_e values may also fail to accurately represent attenuation of the discharge signal from the waterfall due to the complexity of the integrated discharge sources—while the spectral peak in discharge appears to be dominated by the waterfall (section 5.4), the higher frequencies may still be dominated by nearer sources, which would correspond with r and Q values nearly identical to those estimated for the transport signal.

5.6. Applications and Next Steps

Because precipitation and water discharge are significantly easier and less costly to monitor than coarse sediment transport, our results represent a potential application for low cost in field monitoring of sediment transport. If transport data cannot be collected for the initial calibration of coefficients c_f, then calibrating and subtracting out the discharge and precipitation portions of the seismic signal ($a_f Q + b_f p$) will still isolate the transport signal, allowing qualitative monitoring of bed load through relative changes in the transport

signal. If enough bed load transport data can be obtained to calibrate c_f, then our method can provide quantitative estimates of transport rates, q_s. As discussed in section 5.3, our coefficient calibrations appear reasonable compared to previous studies. However, it is likely that the exact spectra (coefficients) we have regressed here are heavily influenced by local variables such as stream geometry, substrate, vegetation, and bed/mobile grain shapes and sizes. The variation between precipitation spectra at our three seismometers no more than 2 m apart, for example, speaks to the importance of these local conditions. Hence, we recommend that future studies perform their own site-specific calibration of coefficient spectra to calculate sediment transport in other streams, rather than attempting to use our spectra in settings for which they may be inaccurate.

While this study used cumulative 10 min resolution data from geophone plates, calibration of c_f could also be achieved using measurements with lower sampling rates, such as sediment traps. Calibration also need not be performed over a single storm, as we have done here, provided a sufficiently wide range of transport rates are sampled. However, additional calibration may be necessary if the relationship between observed seismic power and transport rates, discharge, or precipitation evolves. This could occur, for example, if significant reworking of the channel bed, morphology, or surroundings (e.g., vegetation) causes changes in attenuation (e.g., due to compaction, deposition or erosion), source-receiver distance (e.g., due to thalweg migration), or the source signal generated by a given rate of bed load transport, discharge, or precipitation. It is not yet known how bed evolution during floods may alter the coefficient spectra, but the relatively minor reorganization of the Erlenbach's alluvial bed throughout the 2 month study period did not appear detrimental to our sediment transport predictions following the first calibration storm.

Further experimental and theoretical research is needed to explore the variability of these spectra in different settings and after bed evolution, as well as the site-dependent effects of attenuation. If such research is able to identify a more generalized transport source spectrum (i.e., before attenuation), then the initial calibration of transport spectra may become less important for quantitative estimates, and site-specific attenuation (i.e., the Green's function) may be empirically calibrated using standard seismic techniques. Additional work to constrain the typical values of seismic parameters, such as the quality factor Q in various fluvial substrates, could also enable the eventual use of theoretical Green's functions to accurately estimate attenuation without any calibration of c_f. More work is also needed to model nonlinearity in the relationships between seismic power and discharge, precipitation, and transport. In particular, nonlinear models could be better constrained by the addition of data for higher discharges when calibrating a_f and including transport data for smaller grains near the threshold of motion (e.g., where q_o is fractionally larger) when calibrating c_f. Experimentation with seismic array geometry is also needed; while our unintentionally oblique array orientation proved serendipitous in identifying a potential source of the discharge signal, a channel-perpendicular array may be advantageous due to the path alignment to the nearest point in the channel or thalweg. Conversely, channel-parallel arrays may be able to provide insight on transient transport phenomena, such as the migrating sediment pulse captured by *Roth et al*. [2014].

6. Conclusion

We have shown here that seismic spectra observed near a river contain useful information about discharge, precipitation, and, most importantly, bed load transport. These results address the long-standing need for passive, high time resolution bed load monitoring methods. Regression of seismic spectra with 2 months of precipitation and water discharge data and bed load transport data over a calibration period of a single storm identified the spectral contributions of each process and enabled the estimation of transport for subsequent periods with only the precipitation, water discharge, and seismic data. Our estimated bed load sediment transport rates are reasonable for the highest recorded fluxes but overpredict at low fluxes when compared to the number of impulses recorded by the geophones. However, we suggest that this reflects the ability of the seismometers to register the transport of small grains below the geophones' recording threshold ($D \sim 1$ cm), which generate proportionally more of the signal at smaller fluxes.

Based on our regressed coefficient spectra, the signal generated by rainfall at the Erlenbach appears to be broadband over our entire range of observed frequencies (~16–480 Hz) and varies significantly between seismometers, most likely due to site-specific factors influencing the impact of raindrops on the ground. The seismic responses to water discharge and bed load sediment transport peak in overlapping, nearly

identical frequency bands between roughly 16 and 100 Hz. Higher-frequency power from both processes has been attenuated nearly completely by the time it reaches the nearest seismometer, ~4 m from the channel thalweg (<2 m from the channel bank). At that seismometer, discharge produces seismic PSD maxima at 44–49 Hz, while power generated by bed load transport peaks at 44–46 Hz. We further find that the water discharge signal is strongest in the vertical and channel-parallel (horizontal) components, while bed load sediment transport causes ground motion predominantly in the channel-parallel direction at the seismometer closest to the river.

The methods we have presented here represent a valuable first step in using calibrated seismic spectra to monitor bed load transport rates. With additional research on these topics, seismic regression has the potential to become a convenient and widely applicable approach to monitoring sediment transport in the future.

Acknowledgments

We thank Victor Tsai, Nicole Gasparini, and one anonymous reviewer for helping to evaluate and improve this manuscript, and we gratefully acknowledge the contributions and assistance of Claire Masteller, Alex Beer, Johannes Schneider, Carlos Wyss, Claudia Bieler, Nicolas Zogg, Bruno Fritschi, Jon Perkins, Leonard Sklar, Jim Kirchner, Thorne Lay, Daniel Sampson, Ed Boring, Heather Deshon, Rob Laber, Mikael Witte, Kerri Johnson, Alex Nereson, Allison Pfeiffer, and David Santaniello. We are also grateful for the support of Pnina Miller, Noel Barstow, George Slad, Jackie Gonzales, Mouse Reusch, Katherine Anderson, and other members of the PASSCAL Data, Training, and Logistics Groups. This work was supported by NSF Geomorphology and Land Use Dynamics grant EAR 1148488. The seismic instruments used in this study were provided by the Incorporated Research Institutions for Seismology (IRIS) through the PASSCAL Instrument Center at New Mexico Tech. Data collected will be available through the IRIS Data Management Center. The facilities of the IRIS Consortium are supported by the National Science Foundation under Cooperative Agreement EAR-1261681 and the DOE National Nuclear Security Administration.

References

Aki, K., and P. Richards (2002), *Quantitative Seismology*, 2nd ed., Univ. Sci. Books, Sausalito, Calif.

Aster, R. C., B. Borchers, and C. H. Thurber (2011), *Parameter Estimation and Inverse Problems*, 2nd ed., Academic Press, San Diego, Calif.

Badoux, A., J. M. Turowski, L. Mao, N. Mathys, and D. Rickenmann (2012), Rainfall intensity-duration thresholds for bedload transport initiation in small Alpine watersheds, *Nat. Hazards Earth Syst. Sci.*, *12*(10), 3091–3108, doi:10.5194/nhess-12-3091-2012.

Bagnold, R. A. (1966), An approach to the sediment transport problem General Physics Geological Survey, Prof. paper.

Barrière, J., A. Oth, R. Hostache, and A. Krein (2015), Bed load transport monitoring using seismic observations in a low-gradient rural gravel bed stream, *Geophys. Res. Lett.*, *42*, 2294–2301, doi:10.1002/2015GL063630.

Beer, A. R., J. M. Turowski, B. Fritschi, and D. H. Rieke-Zapp (2015), Field instrumentation for high-resolution parallel monitoring of bedrock erosion and bedload transport, *Earth Surf. Processes Landforms*, *40*, 530–541, doi:10.1002/esp.3652.

Bogen, J., and K. Møen (2003), Bed load measurements with a new passive acoustic sensor, in *Erosion and Sediment Transport Measurement in Rivers: Technological and Methodological Advances*, vol. 283, edited by J. Bogen et al., pp. 181–192, IAHS, Wallingford, England.

Bunte, K., and S. R. Abt (2005), Effect of sampling time on measured gravel bed load transport rates in a coarse bedded stream, *Water Resour. Res.*, *41*, W11405, doi:10.1029/2004WR003880.

Burtin, A., L. Bollinger, J. Vergne, R. Cattin, and J. L. Nabelek (2008), Spectral analysis of seismic noise induced by rivers: A new tool to monitor spatiotemporal changes in stream hydrodynamics, *J. Geophys. Res.*, *113*, B05301, doi:10.1029/2007JB005034.

Burtin, A., J. Vergne, L. Rivera, and P. Dubernet (2010), Location of river-induced seismic signal from noise correlation functions, *Geophys. J. Int.*, *182*(3), 1161–1173.

Burtin, A., R. Cattin, L. Bollinger, J. Vergne, P. Steer, A. Robert, N. Findling, and C. Tiberi (2011), Towards the hydrologic and bed load monitoring from high-frequency seismic noise in a braided river: The "torrent de St Pierre", French Alps, *J. Hydrol.*, *408*(1–2), 43–53, doi:10.1016/j.jhydrol.2011.07.014.

Chao, W. A., Y. M. Wu, L. Zhao, V. C. Tsai, and C. H. Chen (2015), Seismologically determined bedload flux during the typhoon season, *Sci. Rep.*, *5*(8261), doi:10.1038/srep08261.

Fredse, J., and R. Deigaard (1992), in *Mechanics of Coastal Sediment Transport*, *Adv. Ser. on Ocean Eng.*, vol. 3, edited by P. L. F. Liu, World Sci., Hackensack, N. J.

Gimbert, F., V. C. Tsai, and M. P. Lamb (2014), A physical model for seismic noise generation by turbulent flow in rivers, *J. Geophys. Res. Earth Surf.*, *119*, 2209–2238, doi:10.1002/2014JF003201.

Govi, M., F. Maraga, and F. Moia (1993), Seismic detectors for continuous bed-load monitoring in a gravel stream, *Hydrol. Sci. J.*, *38*(2), 123–132, doi:10.1080/02626669309492650.

Gray, J. R., J. B. Laronne, and J. D. G. Marr (2010), Bedload-surrogate monitoring technologies *U.S. Geol. Surv. Sci. Invest. Rep., 2010–5091*, US Geol. Surv., Reston, Va. [Available at http://pubs/usgs.gov/sir/2010/5091.]

Hsu, L., N. J. Finnegan, and E. E. Brodsky (2011), A seismic signature of river bedload transport during storm events, *Geophys. Res. Lett.*, *38*, L13407, doi:10.1029/2011GL047759.

Huang, C. J., H. Y. Yin, C. Y. Chen, C. H. Yeh, and C. L. Wang (2007), Ground vibrations produced by rock motions and debris flows, *J. Geophys. Res.*, *112*, F02014, doi:10.1029/2005JF000437.

Hunter, S. C. (1957), Energy absorbed by elastic waves during impact, *J. Mech. Phys. Solids*, *5*(3), 162–171, doi:10.1016/0022-5096(57)90002-9.

Lamb, M. P., W. E. Dietrich, and L. S. Sklar (2008), A model for fluvial bedrock incision by impacting suspended and bed load sediment, *J. Geophys. Res.*, *113*, F03025, doi:10.1029/2007JF000915.

Leopold, L. B., and W. W. Emmett (1977), 1976 bedload measurements, East Fork River, Wyoming, *Proc. Natl. Acad. Sci. U.S.A.*, *74*(7), 2644–2648, doi:10.1073/pnas.74.7.2644.

McLaskey, G. C., and S. D. Glaser (2010), Hertzian impact: Experimental study of the force pulse and resulting stress waves, *J. Acoust. Soc. Am.*, *128*(3), 1087–1096, doi:10.1121/1.3466847.

Meyer-Peter, E., and R. Müller (1948), Formulas for bedload transport, in *Proceedings of the 2nd Meeting of the International Association for Hydraulic Structures Research*, pp. 39–64, International Association for Hydraulic Structures Research, Delft, Netherlands.

Molnar, P., A. L. Densmore, B. W. McArdell, J. M. Turowski, and P. Burlando (2010), Analysis of changes in the step-pool morphology and channel profile of a steep mountain stream following a large flood, *Geomorphology*, *124*, 85–94, doi:10.1016/j.geomorph.2010.08.014.

Nitsche, M., D. Rickenmann, J. W. Kirchner, J. M. Turowski, and A. Badoux (2012), Macroroughness and variations in reach-averaged flow resistance in steep mountain streams, *Water Resour. Res.*, *48*, W12518, doi:10.1029/2012WR012091.

Pruppacher, H. R., and J. D. Klett (1997), *Microphysics of Clouds and Precipitation*, 2nd ed., pp. 963, Springer, Dordecht, Netherlands, doi:10.1007/978-0-306-48100-0.

Recking, A., F. Liébault, C. Peteuil, and T. Jolimet (2012), Testing bedload transport equations with consideration of time scales, *Earth Surf. Processes Landforms*, *37*, 774–789, doi:10.1002/esp.3213.

Rickenmann, D. (1997), Sediment transport in Swiss torrents, *Earth Surf. Processes Landforms*, *22*, 937–951.

Rickenmann, D., and B. Fritschi (2010), Bedload transport measurements using piezoelectric impact sensors and geophones, in *Bedload-Surrogate Monitoring Technologies*, *US Geol. Sur. Sci. Invest. Rep. 2010–5091*, edited by J. R. Gray et al., pp. 185–194, U.S. Geol. Surv., Reston, Va.

Rickenmann, D., and B. W. McArdell (2007), Continuous measurement of sediment transport in the Erlenbach stream using piezoelectric bedload impact sensors, *Earth Surf. Processes Landforms*, *32*(9), 1362–1378, doi:10.1002/esp.1478.

Rickenmann, D., J. M. Turowski, B. Fritschi, A. Klaiber, and A. Ludwig (2012), Improved sediment transport measurements in the Erlenbach stream including a moving basket system, *Earth Surf. Processes Landforms*, *37*, 1000–1011, doi:10.1002/esp.3225.

Rickenmann, D., et al. (2014), Bedload transport measurements with impact plate geophones: Comparison of sensor calibration in different gravel-bed streams, *Earth Surf. Processes Landforms*, *39*(7), 928–942, doi:10.1002/esp.3499.

Roth, D. L., N. J. Finnegan, E. E. Brodsky, K. L. Cook, C. P. Stark, and H. W. Wang (2014), Migration of a coarse fluvial sediment pulse detected by hysteresis in bedload generated seismic waves, *Earth Planet. Sci. Lett.*, *404*, 144–153.

Schmandt, B., R. C. Aster, D. Scherler, V. C. Tsai, and K. Karlstrom (2013), Multiple fluvial processes detected by riverside seismic and infrasound monitoring of a controlled flood in the Grand Canyon, *Geophys. Res. Lett.*, *40*, 4858–4863, doi:10.1002/grl.50953.

Schneider, J., J. M. Turowski, D. Rickenmann, R. Hegglin, S. Arrigo, L. Mao, and J. W. Kirchner (2014), Scaling relationships between bedload volumes, transport distances and stream power in steep mountain channels, *J. Geophys. Res. Earth Surf.*, *119*, 533–549, doi:10.1002/2013JF002874.

Sklar, L. S., and W. E. Dietrich (2004), A mechanistic model for river incision into bedrock by saltating bed load, *Water Resour. Res.*, *40*, W06902, doi:10.1029/2012WR012267.

Thorne, P. D. (2014), An overview of underwater sound generated by inter-particle collisions and its application to the measurements of coarse sediment bedload transport, *Earth Surf. Dyn. Discuss.*, *2*, 605–633.

Tsai, V. C., B. Minchew, M. P. Lamb, and J. P. Ampuero (2012), A physical model for seismic noise generation from sediment transport in rivers, *Geophys. Res. Lett.*, *39*, L02404, doi:10.1029/2011GL050255.

Turowski, J. M., and D. Rickenmann (2009), Tools- and cover-effect in bedload transport observations in the Pitzbach, Austria, *Earth Surf. Processes Landforms*, *34*, 26–37, doi:10.1002/esp.1686.

Turowski, J. M., E. M. Yager, A. Badoux, D. Rickenmann, and P. Molnar (2009), The impact of exceptional events on erosion, bedload transport and channel stability in a step-pool channel, *Earth Surf. Processes Landforms*, *34*, 1661–1673, doi:10.1002/esp.1855.

Turowski, J. M., A. Badoux, and D. Rickenmann (2011), Start and end of bedload transport in gravel bed rivers, *Geophys. Res. Lett.*, *38*, L04401, doi:10.1029/2010GL046558.

Turowski, J. M., M. Böckli, D. Rickenmann, and A. R. Beer (2013), Field measurements of the energy delivered to the channel bed by moving bed load and links to bedrock erosion, *J. Geophys. Res. Earth Surf.*, *118*, 2438–2450, doi:10.1002/2013JF002765.

Turowski, J. M., C. R. Wyss, and A. R. Beer (2015), Grain size effects on energy delivery to the streambed and links to bedrock erosion, *Geophys. Res. Lett.*, *42*, 1775–1780, doi:10.1002/2015GL063159.

Welch, P. D. (1967), The use of fast Fourier transform for the estimation of power spectra: A method based on time averaging over short, modified periodograms, *IEEE Trans. Audio Electroacoust.*, *15*(2), 70–73.

Wilcock, P. R. (1997), Entrainment, displacement and transport of tracer gravels, *Earth Surf. Processes Landforms*, *22*, 1125–1138.

Wilcock, P. R., and J. C. Crowe (2003), Surface-based transport model for mixed-size sediment, *J. Hydraul. Eng.*, *129*(2), 120–128.

Winkler, W., W. Wildi, J. van Stuijvenberg, and C. Caron (1985), Wägital-Flysch et autres flyschs penniques en Suisse Centrale—Stratigraphie, sédimentologie et comparaisons, *Eclogae Geol. Helv.*, *78*, 1–22.

Wyss, C. R., D. Rickenmann, B. Fritschi, J. M. Turowski, V. Weitbrecht, and R. M. Boes (2014), Bedload grain size estimation from the indirect monitoring of bedload transport with Swiss plate geophones at the Erlenbach stream, in *River Flow 2014*, edited by A. J. Schleiss et al., pp. 1907–1912, CRC Press/Balkema, Leiden, Netherlands.

Wyss, C. R., D. Rickenmann, B. Fritschi, J. M. Turowski, V. Weitbrecht, and R. M. Boes (2016), Measuring bedload transport rates by grain-size fraction using the Swiss plate geophone signal at the Erlenbach, *J. Hydraul. Res.*, doi:10.1061/(ASCE)HY.1943-7900.0001090.